RESEARCH ARTICLE

NANO · MICRO small
www.small-journal.com

Architecture Controls Phonon Propagation in All-Solid Brush Colloid Metamaterials

*Yu Cang, Rebecca Sainidou, Pascal Rembert, Krzysztof Matyjaszewski, Michael Bockstaller, Bartlomiej Graczykowski, and George Fytas**

Brillouin light scattering and elastodynamic theory are concurrently used to determine and interpret the hypersonic phonon dispersion relations in brush particle solids as a function of the grafting density with perspectives in optomechanics, heat management, and materials metrology. In the limit of sparse grafting density, the phonon dispersion relations bear similarity to polymer-embedded colloidal assembly structures in which phonon dispersion can be rationalized on the basis of perfect boundary conditions, i.e., isotropic stiffness transitions across the particle interface. In contrast, for dense brush assemblies, more complex dispersion characteristics are observed that imply anisotropic stiffness transition across the particle/polymer interface. This provides direct experimental validation of phonon propagation changes associated with chain conformational transitions in dense particle brush materials. A scaling relation between interface tangential stiffness and crowding of polymer tethers is derived that provides a guideline for chemists to design brush particle materials with tailored phononic dispersion characteristics. The results emphasize the role of interfaces in composite materials systems. Given the fundamental relevance of phonon dispersion to material properties such as thermal transport or mechanical properties, it is also envisioned that the results will spur the development of novel functional hybrid materials.

1. Introduction

To understand and control the propagation of phonons in materials has emerged as an important requisite to advance innovations in materials that are relevant to a wide range of technology areas. Phonons are carriers of information and energy and are, hence, crucial for applications such as high-frequency filters, telecommunication, optomechanics, and thermal transport.[1–4] Control of the hypersonic band diagram goes beyond understanding high-frequency sound propagation in isotropic media. In the hypersonic frequency range, phonon-matter interaction-physics renders it possible to control phonon propagation via the fabrication of periodic materials with resonant components. The study of phonon propagation in fabricated close-packed face-centered cubic (fcc) colloidal crystals, infiltrated with liquids, goes back to the mid-2000s,[5–10] with the investigation of liquid-embedded colloidal crystal structures.[11–13] The experimentally recorded dispersion curves, $\omega(q)$

Y. Cang
School of Aerospace Engineering and Applied Mechanics
Tongji University
Zhangwu Road 100, Shanghai 200092, China

R. Sainidou, P. Rembert
Laboratoire Ondes et Milieux Complexes UMR CNRS 6294
UNIHAVRE
Normandie University
75 rue Bellot, Le Havre F-76600, France

K. Matyjaszewski
Chemistry Department
Carnegie Mellon University
4400 Forbes Avenue, Pittsburgh, PA 15213, USA

M. Bockstaller
Department of Materials Science and Engineering
Carnegie Mellon University
5000 Forbes Avenue, Pittsburgh, PA 15213, USA

B. Graczykowski
Faculty of Physics
Adam Mickiewicz University
Uniwersytetu Poznanskiego 2, Poznan 61-614, Poland

G. Fytas
Max Planck Institute for Polymer Research
Ackermannweg 10, 55128 Mainz, Germany
E-mail: fytas@mpip-mainz.mpg.de

G. Fytas
Institute of Electronic Structure and Laser
FORTH
N. Plastira 100, Heraklion 70013, Greece

The ORCID identification number(s) for the author(s) of this article can be found under https://doi.org/10.1002/smll.202304157

DOI: 10.1002/smll.202304157

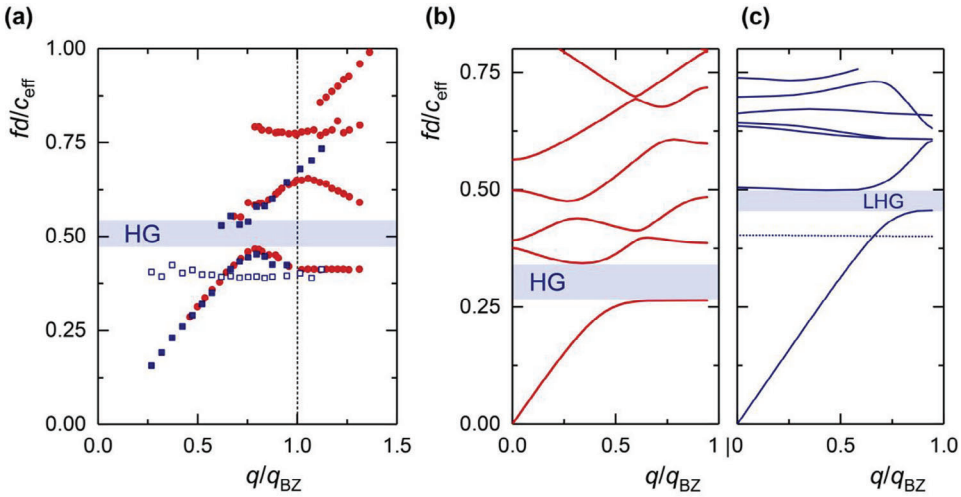

Figure 1. a) Experimental dispersion plot for close-packed PS particles (diameter $d = 307$ nm) infiltrated in PDMS (red filled circles), and silica (SiO_2)-PS GNP assembly (square symbols, $d = 214$ nm) with the empty symbols denoting the dispersionless, highly localized, rotational mode originating from dipole torsional modes of the individual particles; the wavenumber is normalized with respect to q_{BZ} along ΓM direction. Calculated band structure along the [111] fcc high-symmetry direction for the PS opal infiltrated in (fluid) PDMS b) and for the DP980 colloidal crystal c) assuming respectively PBCs and IBCs ($k_T = 0.021$ GPa nm^{-1}). Solid lines: longitudinal bands in (b) and non-degenerate bands including inactive bands in (c); dotted lines: quasi-flat (highly localized) band originating from dipole torsional modes (see main text). Shaded regions denote hybridization gaps of dipole-resonance origin (LHG for longitudinal modes; HG for all modes). The horizontal red arrow in (b) indicates the position of the quadrupolar resonant frequency of the individual PS sphere in PDMS. Note that only non-degenerate bands that correspond to longitudinal phonons are shown (we have omitted transverse phonon modes since they were not observed experimentally in Figure 1a).

(angular frequency vs phonon wavenumber), of such polymer-based colloidal crystals revealed features commonly encountered in ordered metamaterials. These include a linear long-wavelength ($q \to 0$) collective response of the composite characterized by the effective medium speed of sound, $c_{eff} = \omega(q)/q$ and, at higher frequencies, the occurrence of forbidden bands (gaps) related either to the periodicity (Bragg gaps, BG) or to avoided-crossing effects (hybridization gaps, HG) that usually arise from local resonances. The HG occurs at phonon wavelengths much larger than the lattice constant, characteristic feature of phononic metamaterials.[14–16] Interestingly, the measured frequency response of these crystals, revealed substantial deviations from theoretical predictions using common assumptions such as non-overlapping, almost touching particles and perfect boundary conditions (PBCs), i.e., assuming continuity of the displacement field and surface traction across the solid/liquid interfaces.[17] Recent studies[18–21] have shown that the unexpected behavior in these liquid-matrix, close-packed structures arises from colloidal interactions that cannot be neglected and hence need to be considered in the theoretical model.

A representative example of liquid-matrix close-packed soft colloid-based hypersonic phononics, is shown in **Figure 1**. The experimental and theoretical state-of-the-art is illustrated in terms of the reduced band diagram $\omega(q)d/c_{eff}$ versus $q_{\Gamma L}d$ along a high symmetry (ΓL) direction in the fcc structure in Figure 1a,b (red symbols). Here, d is the first-neighbor distance in the fcc lattice that coincides with the particle diameter for close-packed crystals. These fcc crystals assembled from polystyrene (PS) solid colloids and infiltrated with liquid poly(dimethyl siloxane) (PDMS) displayed two bandgaps, one BG and one HG that is attributed to particle resonances. The latter cannot be captured by theory assuming PBCs to describe the solid/liquid interfaces (Figure 1b). For soft colloidal crystals of solid/liquid topology, the full elastodynamic theoretical description assuming non-overlapping particles subject to PBCs underestimates the range of the experimentally retrieved HG (centered at $fd/c_{eff} = 0.51$ in Figure 1a, where $2\pi f = \omega$) by 60%[17,18]; it occurs at $fd/c_{eff} = 0.31$ as evident in Figure 1b (HG in the hatched area). The HG is attributed to the quadrupolar ($l = 2$) resonance of the individual particles (in PDMS), which occurs at $fd/c_{eff} = 0.40$ in Figure 1b (red arrow) and is red-shifted ($fd/c_{eff} = 0.31$) in the fcc crystal due to multiple scattering effects. Additionally, an increased slope in the linear regime is observed experimentally ($c_{eff} = 1670 \pm 30$ m s^{-1} from the slope in Figure 1a), as compared to the lower value ($c_{eff} = 1480$ m s^{-1}) in the theoretical band diagram in Figure 1b. The recently proposed introduction of effective solid/solid interfaces due to colloidal interactions at close-packing increases c_{eff} towards the experimental value and predicts a dipolar-like ($l = 1$) HG, which appears at a higher frequency than the predicted quadrupolar-origin HG (Figure 1b).[18] Yet, the theory does not support the opening of periodicity-based BG, in contrast to the experimental results for fcc colloidal crystals.

The potential of fabricating hypersonic colloidal crystals via self-assembly significantly advanced with the emergence of polymer-grafted nanoparticles (GNP, aka brush particles) as a platform for colloidal (brush) crystal structures.[22] The self-assembly of GNPs results in periodic structures akin to colloidal crystals that constitute a modern example of phononic metamaterials at the nanoscale: the SiO_2 cores self-organize into a fcc lattice and the polymer brushes, playing the role of a host matrix, create a continuum of elastic media with absence of voids. In addition, the matrix content is tunable via the composition of the brush, whereas in classical backfilled colloidal crystals, the matrix content is defined by the available interstitial space (26% in fcc).

Table 1. Molecular characteristics of the PS grafted SiO_2 ($R_c = 57 \pm 2$ nm) nanoparticles (GNP) and their assemblies.

Sample ID	N	σ [nm^{-2}]	d_{TEM} [nm]	d_{cal} [nm][a)]	h_{tot} [nm][b)]	h_{dry} [nm][c)]	ϕ_C	N_{max}[d)]
DP1300	1300	0.53	245 ± 8	218	66 ± 4	47	0.14	670
DP530	530	0.27	163 ± 3	149	25 ± 4	_	0.44	_
DP1170	1170	0.08	140 ± 6	139	13 ± 5	_	0.50	_

a) $\frac{4}{3}\pi\left(\frac{d_{cal}}{2}\right)^3 = \frac{4}{3}\pi R_c^3 + \frac{ZN}{N_k \rho_k}$; $Z = 4\pi R_c^2 \sigma$; b) $h_{tot} = \frac{d_{TEM}}{2} - R_c$; c) $h_{dry} = \frac{d_{cal}}{2} - R_c - \frac{h_{inter}}{2}$; $h_{inter} = \frac{3d_{cal}}{2}(1+x)[1-(1-\frac{4}{3}(\frac{1}{1+x})^2)^{\frac{1}{2}}]$; $x = \frac{2Z}{\pi \rho b^2 d_{cal}}$; d) $N_{max} = (2\sqrt{3}+3)(\rho R_c/\sigma)$; b = 1.8 nm the Kuhn length, $N_k = 7$ monomers/Kuhn segment and $\rho_k = 0.87$ Kuhn segments /nm^3.

Furthermore, the presence of a brush layer alleviates particle core-core contact interactions. The core-to-core separation, d, is facilitated through control of the degree of polymerization, N, and grafting density, σ (number of chains/nm^2) of tethered chains at constant core radius, (inset to Figure 1c). The latter enables the comparison between experimental and theoretical phononic band diagrams. The experimentally recorded, $\omega(q)$, of fcc GNP solids composed of SiO_2 nanoparticles with $R_c = 57 \pm 2$ nm densely grafted with PS (SiO_2-PS, $\sigma = 0.48$ nm^{-2}, $N = 980$; this system is denoted DP980) is shown in Figure 1a. The figure reveals a resonance-induced HG and, additionally, a localized band (empty squares), however, no BG is observed. Remarkably, the experimental dispersion for this GNP ($c_{eff} = 2360$ m s^{-1}, $d = 214$ nm) and the fcc PS/PDMS opal superimpose in the reduced band diagram in Figure 1a. If we focus on the main features of the experimental dispersion diagram for frequencies below the first BG, $\frac{fd}{c_{eff}} \approx 0.65$ (Bragg condition $d_{\Gamma M} = \frac{1}{2}\frac{c_{eff}}{f}$, $d_{\Gamma M} = \frac{4\sqrt{3}}{9}d$) for the two crystal arrays, we observe a good coincidence for the acoustic branch, including the HG region (hatched area in Figure 1a) and a common flat mode occurring at about 0.40 for both systems. The agreement suggests that apart from the (trivial) coincidence at the long-wavelength linear limit, these localized modes scale similarly with $\frac{c_{eff}}{d}$ for both systems. This implies a common origin of the avoided-crossing HG mechanism. Indeed, for the case of GNP assemblies, the frequency of the HG with longitudinal polarization arises from the dipole resonance ($l = 1$) of the individual GNP,[22] and the localized mode (empty squares in Figure 1a) is theoretically represented (dotted flat mode in Figure 1c) assuming anisotropic elasticity across the polymer/particle interface, through imperfect boundary conditions, IBCs (see Experimental Section).[18] Figure 1a confirms our previous argument[18] that a dipole mode is responsible for the HG in close-packed PS colloidal crystals. Note that this mode is typically absent in liquid-matrix crystals of non-overlapping particles (Figure 1b), for which the formation of HG is attributed to quadrupolar ($l = 2$) modes of the individual spheres.[23] We also note that the flat localized mode is the fingerprint of rotational resonances that strongly depend on the boundary conditions applied at the surface of the spherical particles.[22] The anisotropic elasticity, implicit in IBCs, influences their frequency position and has been shown to be a robust parameter in GNP systems with respect to variation of the brush architecture. However, variations in the grafting density quantitatively affect the degree of this anisotropy (see discussion of Figure 5).

So far, there has been only one report[22] on the phononic properties of GNPs and it focused on the tunability of frequency and width of the phononic bandgap by the degree of polymerization N of grafted chains at constant grating density. In this contribution, we demonstrate that grafting density is a second, intriguing control parameter to modulate the phononic band structure in GNP assemblies as it strongly affects the conformation of tethered chains and, thus, interactions within the assembled structures. To reveal the effect of chain packing and conformation, Brillouin light spectroscopy (BLS) provides unique opportunities. Since the phonon wavelength in the vicinity of the HG is larger but close to the particle spacing, access to the band diagram can also index the conformation of the grafted chains. In this work, we utilize BLS to record $f(q)$ at hypersonic (GHz) frequencies in architected SiO_2-PS assemblies with low and high σ and comparable N. Furthermore, to vary the lattice parameter at constant σ and N, plasticization of GNPs is employed. While the structure of $f(q)$ is robust to these changes, unexpected quantitative differences are found between sparsely ($\sigma = 0.08$ chains·nm^{-2}) and densely ($\sigma \approx 0.5$ chains·nm^{-2}) GNP systems notably at similar N. The distinctive features of GNP crystals provide new insights into the role of the molecular architecture on the interactions and phononic properties of GNP-based metamaterial systems.[5,14–16,22] Since the purpose of the present work is to substantiate conclusions from simulation results regarding the origin of the hypersonic phononic bandgap, we selected model systems that were expected to represent best possible matches to the respective boundary conditions ("PBCs" and "IBCs"). A near-identical degree of polymerization ($N \approx 1250$) was used to reduce the number of unknowns, while a third GNP ($N = 530$, $\sigma \approx 0.3$ chains·nm^{-2}) was included as an "intermediate case" for further validation.

2. Results and Discussion

2.1. Spectral Pattern

Table 1 compiles the molecular characteristics of SiO_2-PS GNP and their assemblies studied in this work.[24] The core-core distance d, determined from TEM images, depends on both σ and N, and their relationship could be utilized to evaluate the chain conformations of grafts using the two-layer model (TLM).[24–27] In the TLM model, polymer grafts are ascribed a "dry" inner layer with thickness h_{dry}, that scales according to stretched chain conformations, and an outer layer with interdigitated Gaussian-like chains from neighboring GNPs. The chain stretching energy displays a maximum at N_{max}. The TLM model represents the microstructure of dense GNPs, but fails on sparse systems because of vanishing h_{dry} at low grafting density.[25,28,29] For the dense DP1300 ($\sigma \approx 0.5$ chains·nm^{-2}) system, the TLM predicts

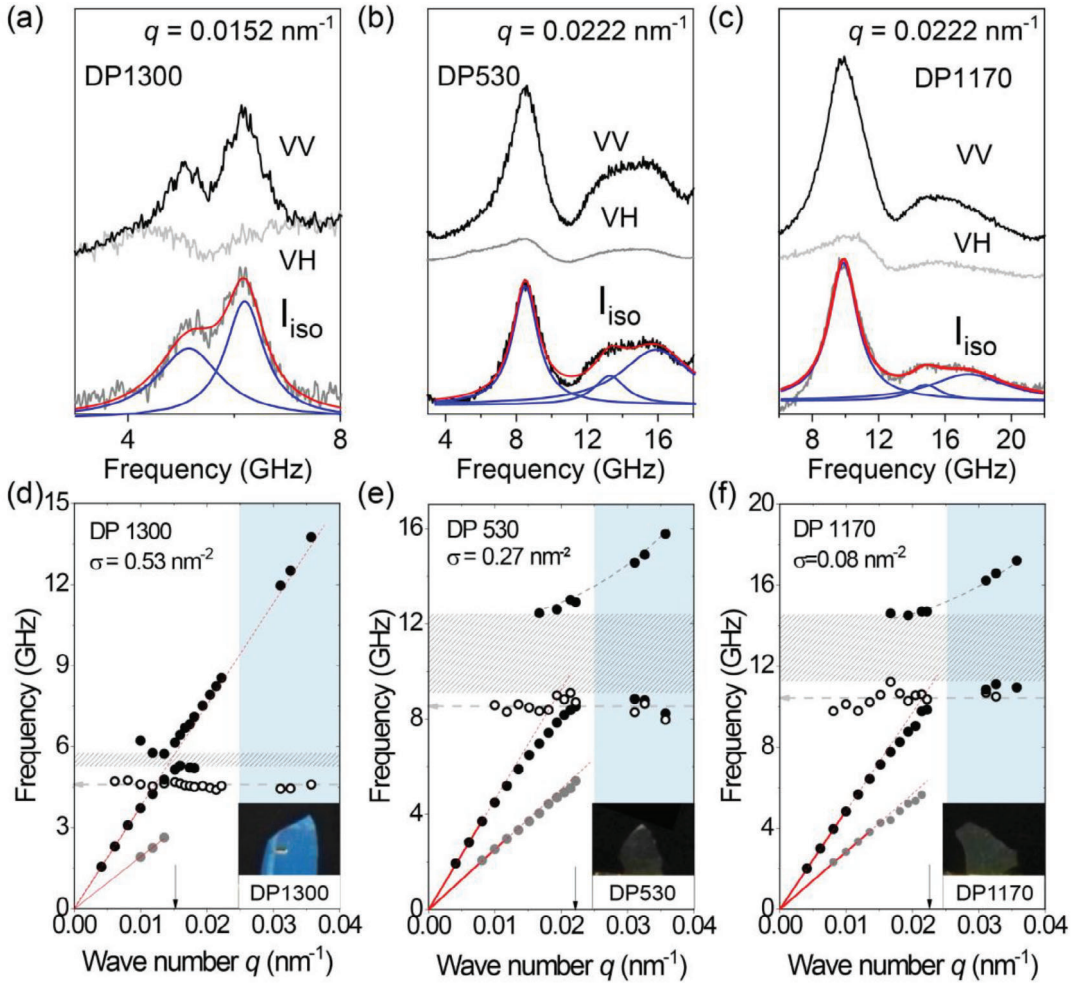

Figure 2. Top panel: experimental BLS spectra of three PS tethered SiO_2 nanoparticle GNP films with different grafting densities, DP1300 ($\sigma = 0.53 nm^{-2}$ in (a)), DP530 ($\sigma = 0.27 nm^{-2}$ in (b)) and DP1170 ($\sigma = 0.08\ nm^{-2}$ in (c)) at a wave vector q (arrows in (d–f)) where a hybridization gap (HG, patterned areas in (d–f)) opens in the dispersion diagrams in (d–f)). The spectra are recorded with VV (black) and VH (grey) polarizations. The isotropic spectra obtained from the subtraction of the VH (depolarized) from the experimental polarized (VV) spectra are represented by Lorentzian lines (red). Bottom panel: experimental dispersion relations of the three systems in (a–c) and their optical images as insets in (d–f). The frequency is obtained from the isotropic spectra recorded at different q's. The direction of q is selected in the transmission and reflection (grey-shaded area) geometries and the magnitude of q is tuned by changing the scattering angle. The HGs denoted by patterned area are clearly observed in each system. The open circles represent the localized mode with q-independent frequency denoted by arrows. The effective medium acoustic modes are represented by red lines in the low-q regime. Note the dip in the BLS intensity at the frequency inside the gap (minimum DOS).

$h_{dry} = 47$ nm, while for $N > N_{max} \approx 700$, the grafts assume Gaussian chain statistics. The N-dependence of the GNP thickness $h(N) = d/2\text{-}R_c$, shown in Figure S1 (Supporting Information), indicates a crossover from extended (slope ≈ 0.7) to coiled (≈ 0.5) conformation for N higher than ≈ 900 for $\sigma \approx 0.5$ chains·nm^{-2}. The crossover occurs near the value of $N_{max} \approx 700$ at which the stretching energy per chain in DP1300 is maximum. With decreasing σ, the extension of the grafted chains decreases as seen for DP530 ($\sigma \approx 0.27$ chains·nm^{-2}, $h \approx 18$ nm) and DP1170 ($\sigma \approx 0.08$ chains·nm^{-2}, $h \approx 12$ nm) in Figure S1 (Supporting Information). Due to the reduced grafting density, the sparse DP1170 possesses about four times shorter graft thickness than DP1300 despite the similar N. Hence, we focus on these three systems to investigate the influence of chain conformations on phononic properties.

Figure 2a–c exemplifies the polarized (black lines) and depolarized (gray lines) BLS spectra of three systems (DP1300, DP530, DP1170) at a given phonon wavenumber. Representation of the BLS spectra by Lorentzian line shapes (solid lines in Figure 2a–c) yields the phononic band diagram of Figure 2d–f revealing a bandgap at ≈ 5.5 GHz. According to selection rules, longitudinal (transverse) phonons could be probed in the polarized (depolarized) BLS spectra that are recorded with VV-parallel (VH-cross) polarization of the incident and scattered light (see Experimental Section). It is the first time that the transverse phonon branch is recorded in hypersonic colloidal crystals[22] that support shear waves and contribute to the VH spectra. Probing shear waves yields rich experimental dispersion plots and allows to retrieve additional information for comparison with theoretical predictions (including HG and c_{eff}, for instance).

Table 2. Hypersonic phononic characteristics of the assembled PS-SiO_2 GNPs.

Sample ID	ϕ_{PS}	$c_{L,exp}$ [m s^{-1}]	$c_{T,exp}$ [m s^{-1}]	f_{LO} [GHz]	f_G [GHz]	Δf_G [GHz]	$f(1,2)$ [GHz][31]	q_G [nm^{-1}]
DP1300	0.86	2370	1200	4.6 ± 0.2	5.5± 0.1	0.4±0.1	6.0±0.1	0.0153±0.003
DP530	0.56	2900	1540	8.5 ± 0.5	11± 0.3	3.3±0.2	14.3±0.2	0.0222±0.003
DP1170	0.50	3060	1780	10.5±0.6	12.5±0.3	3.3±0.3	14.8±0.2	0.0226±0.002

For the VV-polarized BLS spectra of the three GNPs, the appearance of double-peak at phonon wavelengths Λ ($= 2\pi q^{-1}$) commensurate with the spacing d that is a typical feature of phononic bandgap that is formed by the longitudinal bands.[5,6,22] What appears unexpected is the pattern and the strength of the depolarized VH spectra which, in addition to the anticipated effective medium transverse phonon (Figure S2, Supporting Information), reveal a broad peak with minimum intensity at a frequency f_G (≈ 5.5, 11, and 13 GHz, respectively, for DP1300, DP530, and DP1170), with f_G being q-independent (Figure S3, Supporting Information). Based on the dispersion plots in Figure 2d–f, f_G falls in the middle of the observed bandgap and hence the drop in the BLS intensity reflects the reduced phonon density of states (DOS). This new VH mode contributes to the VV-polarized spectra and results in pronounced shape-asymmetry especially at a low-q regime (Figure S4, Supporting Information). According to Figure 2a for DP1300, this VH mode contribution in the VV spectrum is much stronger than for the two sparse GNPs due to multiple (anisotropic) scattering that increases with the GNP size (Figure S5, Supporting Information). It should be absent in the isotropic $I_{iso}(\omega) = I_{VV}(\omega) - x\, I_{VH}(\omega)$ (with $x \approx 1$) due to longitudinal phonons.[22] The reduced $I_{iso}(\omega)$ of DP1300 is well represented by the sum (red line) of two Lorentzian fits (blue lines) at the bandgap region (Figure 2, top panel), whereas a single Lorentzian representation sufficed for the effective medium acoustic phonons at low q's (linear acoustic regime) (Figure S4, Supporting Information). For DP530 and DP1170, the low contribution of the VH mode to the VV spectra (Figure 2b,c) implies that this mode has mainly transverse polarization. In the gap region, $q_G \approx 0.022$ nm^{-1}, the high-frequency branch is double with a contribution at about 15 GHz, discernible in both VV and VH spectra due to the inevitable backscattering contribution to the transmission scattering geometry. Note that this mode is absent in the reflection geometry (blue hatched area). Thus the analysis of the BLS spectra at $q > q_G$ (arrows in Figure 2, bottom panel) leads to the central feature of the phononic GNPs, the experimental diagram of the three systems in Figure 2d–f. The different phonon dispersions in DP1300 and DP1170 with similar N but very different σ is remarkable and is associated with the different spacing (245–140 nm, Table 1). The latter is also inferred from the optical images (insets in Figure 2d–f) suggesting photonic structures with extinction wavelengths $\lambda_{ext} \simeq 2d(n_{eff}^2 - \sin^2\gamma)^{0.5}$ with n_{eff} and γ being the effective refractive index (≃1.5) and light incidence angle.

2.2. Phonon Band Diagram

The low-q acoustic regime yields the longitudinal (c_L) and transverse (c_T) sound velocities that increase from DP1300 and DP530 to DP1170 (**Table 2**). The enhancement of the sound velocities in DP530 to DP1170 is only in part attributed to the increase (decrease) of the SiO_2 core (PS) fraction, ϕ_c (ϕ_{PS}). In the case of DP1170, the larger extent of brush interdigitation enhances brush interactions and hence the sound velocity.[30] The observed bandgap occurs at $q_G d_{TEM} = 3.2\pm0.1$ compared to $q_{\Gamma L} d_{TEM} = 3.8$, $q_{\Gamma M} d_{TEM} = 4.1$ or $q_{\Gamma K} d_{TEM} = 4.7$, rendering an interference-based Bragg-gap at the Brillouin zone unlikely. Alternatively, resonance-based HG in metamaterials occurs at $\frac{\Lambda}{2} \gtrsim d$, as confirmed from Figure 2a–c yielding to $\Lambda/d \approx 2$, i.e., in the first BZ due to interactions of the effective medium acoustic branch with GNP localized acoustic modes. The new VH mode, being predominantly transverse, is localized in space as indicated by a q-independent (Figure S3, Supporting Information) frequency, f_{LO} in Figure 2d–f; $f_{LO} = 4.6 \pm 0.2$ GHz, 8.5 ±0.5 GHz and 10.5 ± 0.6 GHz in DP1300, DP530 and DP1170, respectively. For the same GNPs, the quadrupolar (1,2) resonance in air occurs at $f(1,2) = 6.0\pm0.1$, 14.3±0.2, and 14.8±0.2 GHz clearly exceeding the corresponding f_{LO} values.[31,32] In the same context, f_G at the center of the gap (≈ 5.5 GHz,11 GHz, and 12.5 GHz) is also red-shifted compared to the $f(1,2)$ of the individual GNPs. Experimentally, the dimensionless frequency, $2\pi f_{LO} d_{TEM}/c_{L,}$ assumes 3.7±0.2 for DP1300 and DP530 and becomes lower, 3.0±0.2, for DP1170. The relative gap width, $\Delta f_G/f_G$ increases from ≈5% to 30% from DP1300 to DP1170 being much stronger than it would be expected from a linear increase of ϕ_C. In this context, the successful superposition of the experimental dispersions in Figure 1a fails near the phononic gap region in the case of DP1170 and DP1300 due to the composition dependence of the gap width (Figure S6, Supporting Information). The band diagrams for DP1300 in Figure 2d and the similarly densely grafted ($\sigma \approx 0.5$ chains·nm^{-2}) DP980 in Figure 1a display the same pattern with very similar values of f_G ($= 0.5\ d/c_{eff}$)= 5.5 GHz and f_{LO} ($= 0.38d/c_{eff}$) = 4.6 GHz. The close similarity between DP1300 and DP980 is consistent with the similar d values 218 and 214 nm, respectively. The slight disparity in the values of N is primarily reflected in the slightly larger core-core separation in the DP1300. The theoretical band diagram of DP980 in Figure 1c captures the experimental f_{LO} by adjusting the tangential stiffness to k_T = 0.021 GPa nm^{-1} ; it corresponds to the tangential stress on the surface divided by the displacement discontinuity. For sufficiently large k_T, the displacement discontinuity vanishes and thus PBCs are recovered (see Theoretical Calculations in Experimental Section).

Prior to the theoretical representation, we examine the effect of swelling of the limiting values of grafting densities at comparable N to tune the dispersion relation through expansion and/or slow-down of the effective medium sound velocities. In the case of the sparse DP1170, swelling should reduce the brush interdigitation and thereby c_L (c_T), whereas for the dense DP1300 the primary

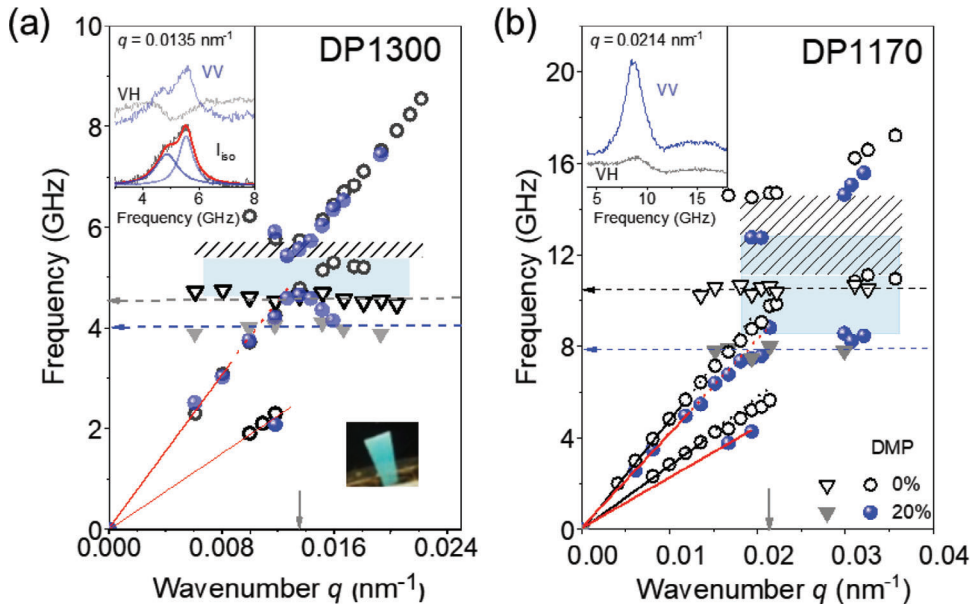

Figure 3. Dispersion relation of a) DP1300 and b) DP1170 swollen with 20 wt.% DMP (solid symbols). For comparison, the phonon dispersion in the pristine GNP films (open symbols) is shown in (a,b). The black and red lines denote the low-frequency acoustic regime of DP1170 and plasticized DP1170, while the blue and black dashed lines are to guide the eyes. The vertical arrows indicate the position of the HG indicated by the hatched and shaded areas, whereas the horizontal lines with arrows indicate the frequency f_{LO} of the flat mode. Insets: Experimental VV (blue) and VH (grey) for the two plasticized samples and optical images of DP1300 with 20% DMP in (a). The isotropic spectra obtained from the subtraction of the VH (depolarized) from the polarized (VV) spectra are represented by Lorentzian lines (red) as in Figure 2a,c.

effect is expected to be an increase of the spacing due to the rather stretched chain graft conformation.[33,34] Based on **Figure 3a**, the effective medium sound velocity in DP1300 remains virtually unchanged but both f_{LO} and q_G (parallel and vertical arrows) decrease upon 20% DMP plasticization. In fact, the frequency f_G also drops as seen from the minimum of the VH spectrum in the inset of Figure 3a compared to the corresponding spectrum in Figure 2a due to the increased spacing (decreased q_G). Based on the decrease of f_{LO} and q_G, the swelling of DP1300 assumes ≈15% in agreement with the change in the structural color of the photonic films (insets to Figures 2d and 3a). In the case of the plasticized DP1170, only f_{LO} drops by ≈13% (Figures 3b and 2c) which, however, is compensated by a similar (≈15%) decrease of c_L thus resulting in a virtually constant q_G (spacing) suggesting virtually constant $2\pi f_{LO} d_{TEM}/c_{L.}$ The virtual constant spacing in DP1170 upon swelling was also supported by the unchanged color of the film. The theoretical representation of the experimental band diagram should elucidate the nature of the HG and reveal the impact of the internal nanoscopic GNP structure on acoustic wave propagation at GHz frequencies.

2.3. Theoretical Band Diagram

In a first attempt to describe the experimental phononic dispersion in DP1170, we assume continuity of the displacement field across the SiO_2/PS interface, i.e., PBCs. The calculations are performed along the fcc [111] direction (ΓL high-symmetry line of the BZ, this direction is consistent with the typical structure of solution-cast colloidal crystals) and bulk PS sound velocities $c_L = c_L^{(b)} = 2350\ m\ s^{-1}$, $c_T = c_T^{(b)} = 1210\ m\ s^{-1}$ are used. The results in **Figure 4a**, exhibit a typical picture for all-solid phononic fcc arrays with a moderate mismatch between the spherical particle and the matrix surrounding it; here, the PS grafts are assumed to form the host matrix. Longitudinal (dark blue solid lines) and transverse (light blue solid lines) bands with linear behavior at the long-wavelength limit are strongly bent at higher frequencies. In addition, deaf bands (dotted lines) are also present, the lowest of them occurring at ≈10.5 GHz compares with f_{LO}, observed experimentally. In general, deaf (or inactive) bands are eigenmodes that are silent in the transmission geometry involving only elastic waves under specific conditions[17] (See Experimental Section). We should note that the photoelastic mechanism of the BLS renders these bands active in the depolarized spectrum.[22] The origin of this quasi-flat collective mode lies in dipole torsional modes of the individual particles that interact weakly with each other to form a flat resonant band.[22,32] Though the theoretical picture successfully captures f_{LO} and the appearance of a bandgap from 10 to 14 GHz, the experimental c_{eff} for both longitudinal and transverse acoustic branches in DP1170 are underestimated. An increase in the PS graft sound velocities, c_L and c_T, could successfully reproduce the experimental c_{eff}, but leads to a strong blueshift of the flat localized band, f_{LO}, compared to the experimental value (Figure S7, Supporting Information) thus rendering a successful representation of the experimental band diagram of DP1170 impossible.

Similarly, the assumption of PBC's at the particle surface along with bulk PS sound velocities, fail to reproduce the experimental results for DP1300 (Figure 4d). However, a distinct, opposite phenomenology is revealed. The effective medium branches are now slightly overestimated, and the same stands for the narrow HG centered at ≈6 GHz in Figure 4d. Yet, the most striking

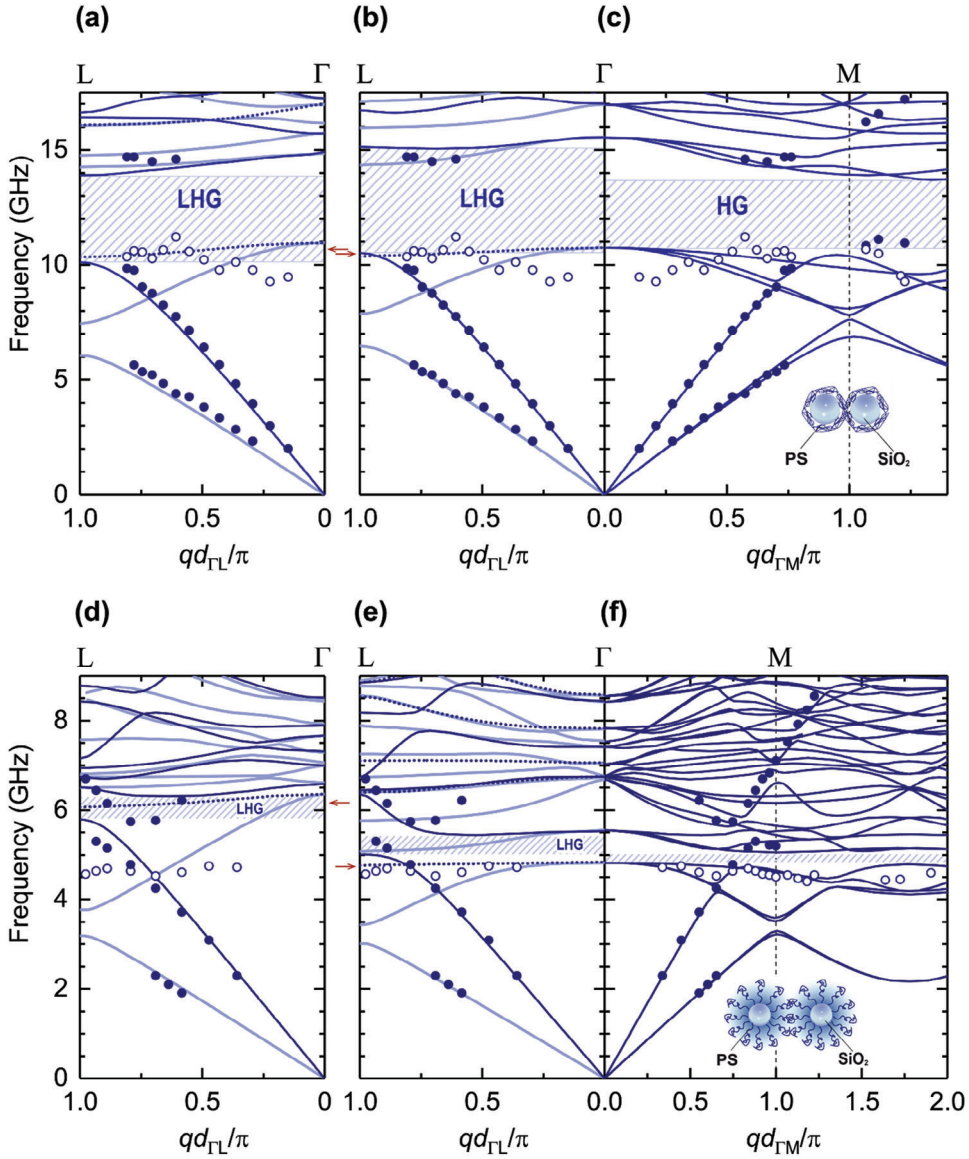

Figure 4. Theoretical band diagram of the a–c) sparsely DP1170 (d = 140 nm) and d–f) densely grafted DP1300 (d = 225 nm) considering PBCs with bulk PS sound velocities ($c_L = c_L^{(b)} = 2350\ m\ s^{-1}$, $c_T = c_T^{(b)} = 1210\ m\ s^{-1}$) along [111] (left column, plots (a,d)), and, IBCs along [111] (middle column, plots (b,e)) and [112] (right column, plots (c,f)); the parameters used for the calculations are: $k_L = 1.16\ GPa\ nm^{-1}$, $k_T = 0.20\ GPa\ nm^{-1}$) with higher than bulk PS sound velocities ($c_L = 1.25\ c_L^{(b)}$, $c_T = 1.35\ c_T^{(b)}$), for DP1170 (plots b,c) and $k_L = 0.615\ GPa\ nm^{-1}$, $k_T = 0.030\ GPa\ nm^{-1}$ with bulk PS sound velocities for DP1300 (plots (e,f)). Solid and open circles indicate the experimental points. Hatched regions denote hybridization gaps (LHG for longitudinal modes; HG for all modes). Along the high symmetry line ΓL of the fcc Brillouin zone (BZ), dark/light solid and dotted blue lines denote non-degenerate (longitudinal, i.e., of Λ_1 symmetry), doubly-degenerated (transverse, i.e., of Λ_3 symmetry) and deaf (i.e., of Λ_2 symmetry) computed bands, respectively. Along [112] that includes the low symmetry line ΓM of the fcc BZ all bands are non-degenerate of mixed character. The position of the flat band of dipole torsional origin is indicated by a red arrow.

deviation between theory and experiment is the position of the flat band predicted theoretically at ≈6.2 GHz, i.e., by ≈50% too high with respect to the experimental value (dotted line vs open circles). This suggests that the larger interparticle distance of DP1300 as compared to DP1170 alone cannot reconcile the spectral differences between both systems. We thus hypothesize that the unique presence of h_{dry} in the case of DP1300 fundamentally alters the phonon dispersion in the brush particle assembly.

To evaluate the role of brush architecture, we next consider high-density GNP arrays for which IBCs that have been shown to successfully describe the dispersion properties.[22] Figure 4b,c and Figure 4e,f show, respectively, the corresponding calculations for DP1170 and DP1300 along fcc [111] (plots b and e) and [112] (plots c and f) directions. When IBCs are adopted to account for elastic displacement discontinuity near the SiO_2/PS interface, the experimental dispersion of DP1170 can be well represented using higher than bulk sound velocities for the PS

grafts, $c_L = 1.25\ c_L^{(b)}$, $c_T = 1.35\ c_T^{(b)}$, and $k_L = 1.16$ GPa nm^{-1}, $k_T = 0.20$ GPa nm^{-1}, for the normal and tangential stiffness, in Figure 4b,c. Similarly, a successful representation is obtained for DP1300, using bulk sound velocities for the PS grafts, and $k_L = 0.615$ GPa nm^{-1}, $k_T = 0.030$ GPa nm^{-1}, for the normal and tangential stiffness, in Figure 4e,f. Two directions are considered, along the high symmetry line ΓL (middle column in Figure 4) and along the low symmetry line ΓM (right column in Figure 4) of the first BZ of the fcc. The latter direction lifts degeneracies in transverse bands but is closer to the experiment, though numerically cumbersome. In general, a comparison between these two directions reveals narrower bandgaps and slightly more dispersive flat bands (whose center is indicated by red arrows) along ΓM. Though the reading of the dispersion plots along ΓM is somewhat complicated (due to the lift of degeneracies of transverse modes with respect to ΓL), this representation is still more accurate and improves the agreement between the theoretical lines and the experimental points.

The frequency of the flat mode is strongly affected and controlled by the tangential stiffness k_T (Figure 4; Figure S7, Supporting Information) and this can be qualitatively understood since this band originates from the torsional motion of the spherical particles, which is sensitive to tangential stiffness. On the other hand, both k_L and k_T affect the general picture of the dispersion in a rather complex manner, thus preventing a straightforward physical interpretation of the complex band structures. We note that the features of the first three acoustic branches (one longitudinal and one, doubly-degenerated transverse) along ΓL (with linear dependence at the long-wavelength limit), including the slope c_{eff} and bending are governed by k_L and k_T, as well as by c_L and c_T of the PS grafts. While for given interparticle distance d, k_T can be determined from experimental results via the flat mode position, its radial counterpart k_L does not have a one-to-one correspondence with experimentally determined features of the dispersion plot. However, we note that with increasing values of k_L and k_T the closer the model becomes to PBCs (i.e, the discontinuity of the displacement field decreases). For this GNP assembly, the polymer grafts, due to the sparse grafting condition, are expected to lack a dry brush region and assume a more "collapsed conformation" to cover the particle surface. This relaxes the discontinuity of the displacement field across the SiO_2 spherical interface and conceivably raises the tangential stiffness of the polymer. For DP1170, the representation of the enhanced c_{eff} requires ≈30% higher PS sound velocities.[30,35]Thus it is the low σ and the high N that control boundary conditions and elasticity ($\approx c_{eff}^2$). For DP1300, the dense counterpart of DP1170, small k_T values are needed (i.e., strong discontinuity of the tangential displacement field across the SiO_2 interface). We attribute the change in k_T to the presence of the dry layer. The effect could bear similarity to previous reports that revealed the presence of a dry layer to impact physical properties such as thermal transport or dielectric breakdown strength of brush particle assembly structures.[36,37]

So far, according to the experimentally recorded band structures of GNP colloidal crystals, two quantities seem to summarize the dispersion properties of these arrays: the effective medium slope, c_{eff}, and the resonant frequency of the flat resonance mode, f_{LO}, both retrieved from BLS experiments. **Figure 5a,b** summarize these key quantities for GNP in the limit of dense-[22] and low-grafting density (present study) respectively, as a function of the first-neighbor distance d. In Figure 5a, c_{eff} is deduced from the theoretical calculation at the long-wavelength limit (left axis) and reveals a decrease with d, similar to the PS propagation velocity used in the calculations. Figure 5a displays the ratio $c_T/c_T^{(b)}$ for transverse waves, shown in the right axis, but similar values are used for the velocities $c_L/c_L^{(b)}$ of longitudinal waves. The more dilute (low ϕ_c) the crystal, the lower the degree of PS speed enhancement is, but for similar N's, the grafting density σ plays a crucial role in differentiating the degree of velocity enhancement needed to describe the experimental data. This can be understood as an indirect evidence that chain conformation dictates a distinct degree of stretching (see, e.g., DP1300 vs DP1170) that alters the stiffness across the polymer/particle interface conformation.[30] In parallel, the decrease in the resonant frequency f_{LO} with d (Figure 5b) manifests a redshift with respect to the theoretically predicted values if PBCs and bulk PS velocities are assumed (dotted line in Figure 5b).

The application of IBCs in the theoretical calculations is necessary to describe f_{LO} in both dense- and sparse-grafting crystals, but again σ is shown to play a crucial role in relaxing these conditions: for low σ the IBCs become less pronounced and the predicted f_{LO} approaches that for PBCs (see, e.g., solid line as a guide to the eye, in Figure 5b). Interestingly, although the dispersion characteristics are found to depend on the grafting density (and hence chain conformation), a robust universal power is found to relate the effective parameter k_T to the resonant frequency of the flat mode, viz. $k_T \approx f_{LO}^{0.41}$ (dotted line in Figure 5c); this power-law variation is also obeyed by the dense GNPs (Figure S8, Supporting Information). As both quantities decrease with particle diameter, d, a trivial dependence $f_{LO} \sim k_T$ would be anticipated. However, Figure 5c suggests a scaling relation, $f_{LO} \sim k_T^{0.41}$ and hence the exponent (<1) implies a strong decrease of k_T with d than f_{LO}, which besides d also depends on the c_{eff} (Figure 5a,b). The inherent dependence of c_{eff} and k_T on the GNP architecture renders a solid account for the scaling in Figure 5c ambiguous and certainly, the underlying physical mechanism that governs this dependence should be elucidated in the future, combining systematic chemical data, microstructure models and multiple-scattering analysis. An instructive representation of the relation between k_T and GNP architecture is in terms of the degree of monomer crowding on the particle surface, which can be represented by the parameter $x = 4R_c^2\sigma/(\rho_K b^2 R_{tot}) = 4R_c^2\sigma/(\rho_K b^2)/[R_c^3+3R_c^2\sigma N/\rho]^{1/3}$ with ρ_K and R_{tot} denoting the Kuhn segment density and the total GNP radius.[25,26] The value of x is a measure of the graft conformation as larger values indicate more pronounced deviation from the equilibrium random coil statistics. The variation of k_T with x is depicted in Figure 5d. A clear trend applying for DP1170 (high k_T value, PBC) and DP1300 (low k_T value, IBCs) is indicated by the solid blue line and relates to the strong increase of polymer crowding with σ.

The degree of polymerization as well as grafting density affect interactions and brush interdigitation. This has been the subject of extensive experimental[28–30,38,39] and theoretical analysis.[25–27,40] Our analysis and assignment of brush

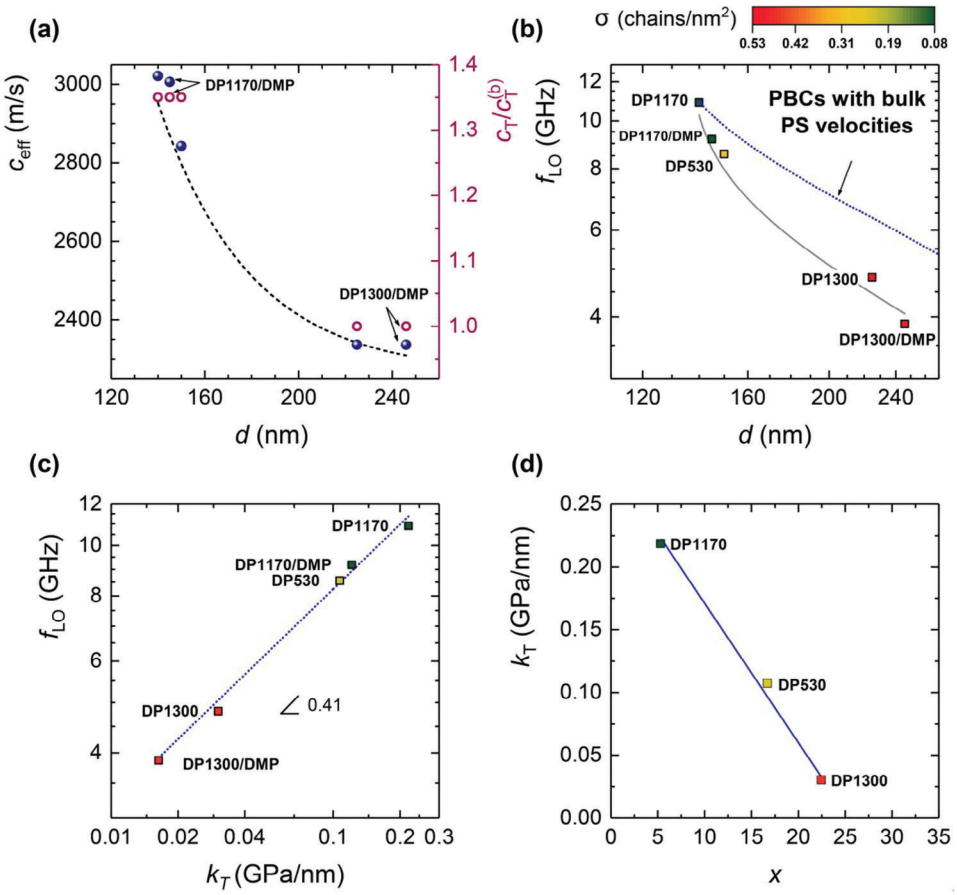

Figure 5. a) Evolution of the effective medium slope for the different colloidal SiO_2-PS GNP assemblies (filled symbols, left axis) and of the enhanced transverse velocity ratio for PS (open symbols, right axis) as a function of the interparticle distance, $d = d_{cal}$ (Table 1), showing a non-linear decay with increasing PS filling fraction (dashed curve is a guide to the eye). b) Redshifted variation of the localized-mode frequency, f_{LO}, for the GNP colloids with increasing distance d. Blue dotted line denotes the flat mode frequency for a fcc crystal calculated along ΓL (taken at the middle of the BZ) assuming PBCs and bulk velocities for PS; solid gray line: interpolated curve for the various samples. c) Power-law variation of the localized-mode frequency with the tangential stiffness k_T. d) The tangential stiffness k_T as a function of the crowding parameter for the DP1170, DP530 and DP1300 with decreasing σ. In (b,c), all scales are logarithmic, symbols are color-indexed with the grafting-chain density value of the corresponding labeled samples.

regimes is based on theory (TLM)[25–27] and molecular dynamics simulations[30] of brush microstructures. The analysis motivates the choice of the material systems, which are in the dense (DP1300) and sparse (semidilute) (DP1170 and DP530) regime. The results support the proposed brush regimes. For example, strong interpenetration at low grafting density (DP1170), renders perfect-like boundary conditions, blueshifting of the frequency of local resonance f_{LO} and enhancement of the elasticity ($\approx c_{eff}^2$) as summarized in Figure 5. The ubiquitous role of "brush particle-type structures" across soft and biomaterial applications (such as micellar/vesicular structures, protein hybrids, etc.) suggests that our results could be applied to a wider class or material systems. For example, the context of chain conformation tunability, planet (star polymers)-satellite (nanoparticles) nanoobjects[41] can also be an alternative platform for chain conformation engineering. Given their smaller size compared with the present GPN's, phononic behavior is anticipated at much higher (hundreds of GHz) frequencies, relevant for nanophononics.[4] However, the fabrication of assembled solid structures is a prerequisite.

3. Concluding Remarks

Our results demonstrate that brush architecture exerts a profound impact on the phonon dispersion characteristics of brush particle assembly structures. In sparse brush systems, the phonon dispersion displays similarity to regular two-component colloidal structures (such as polymer-embedded colloidal crystal assemblies). The phonon dispersion relation is well represented by elastodynamic theory under the assumption of PBCs, indicating an isotropic distribution of stiffness across the particle/polymer interface. This is consistent with the expected isotropic "mushroom-type" conformation of tethered chains and also applies to backfilled colloidal crystal structures. In contrast, dense brush particle assemblies feature more complex dispersion characteristics. The full elastodynamic theory reveals that the different dispersion characteristics arise from stiffness anisotropy across the particle/polymer interface (viz. IBCs). This is consistent with the predicted (and experimentally observed) orientation of chains due to crowding across a region adjacent to the interface (i.e., the "dry brush" region). Here, elastodynamic

theory reveals a robust scaling relation between (tangential) interface stiffness and a "crowding parameter" that describes the packing constraints of polymer tethers across the interface. Our results thus provide not only insights into microstructure-property relations in brush and brush-particle based systems that could inspire the future development of novel functional materials but also a guideline for chemists to design brush-based materials with engineered phonon dispersion characteristics. The systematic variation of brush architecture (degree of polymerization, grafting density as well as dispersity) of tethered chains would be a very interesting extension of the present work. Open questions relate to the role of chain dispersity and composition (e.g., uni- vs bimodal) that might yet present additional degrees of freedom to tune the phononic characteristics of brush particle-based materials.

4. Experimental Section

Samples: The SiO_2-PS GNP with a radius $R_c = 57 \pm 2$ *nm* of the SiO_2 NP were synthesized via surface-initiated atom transfer radical polymerization (SI-ATRP) following previously published routines.[42,43] By casting the PS-grafted nanoparticles out of their dispersion in toluene and subsequently performing thermal treatment to exclude the structural defects, highly ordered films with a thickness between 50 and 100 µm were obtained. The low degree of size dispersity allows densely tethered SiO_2-PS GNPs to self-assemble into an fcc structure as confirmed by TEM images.[30,31] The grating density, σ, and degree of polymerization, N, of tethered PS chains could be systematically varied in a wide range to tailor the segmental distribution and hence interactions between particles.[44] The molecular characteristics of SiO_2-PS GNP and their assemblies studied in this work (sample ID: DP-*N*) are listed in Table 1.

Brillouin Light Spectroscopy: Brillouin light spectroscopy (BLS) probes the spectrum of the inelastically scattered laser beam by thermally activated phonons with wavevector $\mathbf{k}$, which equals to scattering wave vector $\mathbf{q} = \mathbf{k_s}\text{-}\mathbf{k_i}$ defined by the scattering geometry with $\mathbf{k_s}$ and $\mathbf{k_i}$ being wave vector of scattered and incident lights. The magnitude of $q = \frac{4\pi sin\alpha}{\lambda}$ in the transmission geometry is tuned by the incident angle α and independent from refractive index n as α ($= \theta/2$) is half of the scattering angle θ, where $\lambda = 532$ nm is the wavelength of the incident light. In contrast, in the reflection geometry, $q = \frac{4\pi\sqrt{n^2-\sin^2\alpha}}{\lambda}$ depends on both α and n. The coupling between incident photon and thermal phonons is demonstrated in the frequency shift $f(q)$ of the BLS spectrum at hypersonic (GHz) frequencies, resolved by a high-resolution tandem Fabry–Perot interferometer (JRS Instruments). The longitudinal and transverse spectra are selected by parallel (VV) and cross (VH) polarizations respectively, where the V and H denote the vertically and horizontally polarized light relatively to the scattered plane.

Theoretical Calculations: All band structure calculations concerning the fcc colloids in this study were performed using a first-principles full elastodynamic multiple-scattering theory[45,46] that takes into account all interactions of the multipole expansions of the elastic field between particles, provided they were non-overlapping (i.e., almost touching, for close-packed structures). Across the spherical particle interface boundary conditions were applied; for all-solid colloids, one usually considers[45,46] perfect boundary conditions (PBCs), i.e., continuity of both the displacement field vector $\mathbf{u}$ and surface traction $\boldsymbol{\tau}$ components across the interface. Imperfect boundary conditions (IBCs) that introduce a discontinuity $\Delta\mathbf{u}$ of displacement field across the particle interface could also be considered to describe interphases instead of idealized (perfect) boundaries. In that case, the induced $\Delta\mathbf{u}$ equals the still continuous surface traction $\boldsymbol{\tau}$, divided by an appropriate stiffness coefficient k, that was different for the displacement components, normal (k_L) and tangential (k_T) to the spherical surface.[22,32,47] When $k_T, k_L \to \infty$, the displacement discontinuity $\Delta\mathbf{u}$ vanishes and the PBCs are recovered.

The dispersion relation $\omega(q)$ of the elastic eigenmodes (band structure) in these colloidal assemblies of spherical particles was calculated either along the [111] direction, which was a high-symmetry line (ΓL) of the BZ, or along the low-symmetry line ΓM, which better describes the experimental setup.[6] Since ΓM was close to ΓL, small deviations were expected between the dispersion diagrams along these directions,[22] including lifting of degeneracies for the double (transverse) bands. The study recalled that for systems organized in an fcc structure with a solid host matrix surrounding the spherical particles, three kinds of bands exist along the [111] direction: transverse bands that were doubly degenerate (Λ_3 symmetry), longitudinal bands that were nondegenerated (Λ_1 symmetry), and deaf (inactive) bands, which were nondegenerated (Λ_2 symmetry).[22] Classification of bands as deaf is related to transmission experiments, with non-excitation of the corresponding eigenmodes of the infinite crystal by an external elastic wave incident normally on the finite slab of the crystal for symmetry reasons. These bands might become active (though they transmit energy weakly), under a slight off-normal excitation. In the case of BLS experiments, several reasons could lead to the activation of these bands, such as the spreading of the exciting beams, as well as the elastic-optic coupling that could trigger optical activity.

Supporting Information

Supporting Information is available from the Wiley Online Library or from the author.

Acknowledgements

Y.C. and G.F. acknowledge financial support by the ERC AdG SmartPhon (Grant No. 694977). Y.C. acknowledges the financial support by the National Natural Science Foundation of China (Grant No. 12102304), the Fundamental Research Funds for the Central Universities and "Germany Strategy 2.0" of Tongji University (Grant No. ZD2023021). M.B. thanks the National Science Foundation grant DMR 2209587 for financial support and B.G. acknowledges the National Science Centre of Poland (NCN) by the OPUS grant 2021/41/B/ST5/03038.

Open access funding enabled and organized by Projekt DEAL.

Conflict of Interest

The authors declare no conflict of interest.

Data Availability Statement

The data that support the findings of this study are available from the corresponding author upon reasonable request.

Keywords

acoustic phonons, brillouin light scattering, brush nanoparticles, mechanical properties, multiple-scattering theory

Received: May 17, 2023
Revised: October 27, 2023
Published online: November 16, 2023

[1] M. Maldovan, *Nature* **2013**, *503*, 209.
[2] P. A. Deymier, *Acoustic Metamaterials and Phononic Crystals*, Vol. *173*, Springer Science & Business Media, Springer, Berlin **2013**.

[3] A. Adibi, A. Khelif, *Phononic Crystals: Fundamentals and Applications*, Springer, Berlin **2016**.
[4] M. Jansen, W. A. Tisdale, V. Wood, *Nat. Mater.* **2023**, *22*, 161.
[5] T. Still, W. Cheng, M. Retsch, R. Sainidou, J. Wang, U. Jonas, N. Stefanou, G. Fytas, *Phys. Rev. Lett.* **2008**, *100*, 194301.
[6] W. Cheng, J. Wang, U. Jonas, G. Fytas, N. Stefanou, *Nat. Mater.* **2006**, *5*, 830.
[7] T. Gorishnyy, C. K. Ullal, M. Maldovan, G. Fytas, E. L. Thomas, *Phys. Rev. Lett.* **2005**, *94*, 115501.
[8] A. V. Akimov, Y. Tanaka, A. B. Pevtsov, S. F. Kaplan, V. G. Golubev, S. Tamura, D. R. Yakovlev, M. Bayer, *Phys. Rev. Lett.* **2008**, *101*, 033902.
[9] G. Zhu, N. Z. Swinteck, S. Wu, J. S. Zhang, H. Pan, J. D. Bass, P. A. Deymier, D. Banerjee, K. Yano, *Phys. Rev. B* **2013**, *88*, 144307.
[10] A. S. Salasyuk, A. V. Scherbakov, D. R. Yakovlev, A. V. Akimov, A. A. Kaplyanskii, S. F. Kaplan, S. A. Grudinkin, A. V. Nashchekin, A. B. Pevtsov, V. G. Golubev, T. Berstermann, C. Brüggemann, M. Bombeck, M. Bayer, *Nano Lett.* **2010**, *10*, 1319.
[11] J. H. Lee, C. Y. Koh, J. P. Singer, S. J. Jeon, M. Maldovan, O. Stein, E. L. Thomas, *Adv. Mater.* **2014**, *26*, 532.
[12] T. Vasileiadis, J. Varghese, V. Babacic, J. Gomis-Bresco, D. Navarro Urrios, B. Graczykowski, *J. Appl. Phys.* **2021**, *129*, 160901.
[13] Y. Cang, Y. Jin, B. Djafari-Rouhani, G. Fytas, *J. Phys. D: Appl. Phys.* **2022**, *55*, 193002.
[14] Z. Liu, X. Zhang, Y. Mao, Y. Y. Zhu, Z. Yang, C. T. Chan, P. Sheng, *Science* **2000**, *289*, 1734.
[15] T. Still, M. Oudich, G. K. Auerhammer, D. Vlassopoulos, B. Djafari-Rouhani, G. Fytas, P. Sheng, *Phys. Rev. B* **2013**, *88*, 094102.
[16] F. Lemoult, N. Kaina, M. Fink, G. Lerosey, *Nat. Phys.* **2013**, *9*, 55.
[17] I. E. Psarobas, A. Modinos, R. Sainidou, N. Stefanou, *Phys. Rev. B* **2002**, *65*, 064307.
[18] Y. Cang, R. Sainidou, P. Rembert, G. Magnabosco, T. Still, N. Vogel, B. Graczykowski, G. Fytas, *J. Phys. Chem. B* **2022**, *126*, 6575.
[19] M. Abi Ghanem, A. Khanolkar, S. P. Wallen, M. Helwig, M. Hiraiwa, A. A. Maznev, N. Vogel, N. Boechler, *Nanoscale* **2019**, *11*, 5655.
[20] B. Graczykowski, N. Vogel, K. Bley, H.-J. Butt, G. Fytas, *Nano Lett.* **2020**, *20*, 1883.
[21] M. Hiraiwa, M. Abi Ghanem, S. P. Wallen, A. Khanolkar, A. A. Maznev, N. Boechler, *Phys. Rev. Lett.* **2016**, *116*, 198001.
[22] E. Alonso-Redondo, M. Schmitt, Z. Urbach, C. M. Hui, R. Sainidou, P. Rembert, K. Matyjaszewski, M. R. Bockstaller, G. Fytas, *Nat. Commun.* **2015**, *6*, 8309.
[23] R. S. Penciu, H. Kriegs, G. Petekidis, G. Fytas, E. N. Economou, *J. Chem. Phys.* **2003**, *118*, 5224.
[24] J. Choi, C. M. Hui, M. Schmitt, J. Pietrasik, S. Margel, K. Matyjazsewski, M. R. Bockstaller, *Langmuir* **2013**, *29*, 6452.
[25] J. Midya, M. Rubinstein, S. K. Kumar, A. Nikoubashman, *ACS Nano* **2020**, *14*, 15505.
[26] S. Y. Chan, M. Jhalaria, Y. Huang, R. Li, B. C. Benicewicz, C. J. Durning, T. Vo, S. K. Kumar, *ACS Nano* **2022**, *16*, 10404.
[27] Z. Wu, S. Pal, S. Keten, *Macromolecules* **2023**, *56*, 3259.
[28] D. Parisi, E. Buenning, N. Kalafatakis, L. Gury, B. C. Benicewicz, M. Gauthier, M. Cloitre, M. Rubinstein, S. K. Kumar, D. Vlassopoulos, *ACS Nano* **2021**, *15*, 16697.
[29] M. Jhalaria, Y. Cang, Y. Huang, B. Benicewicz, S. K. Kumar, G. Fytas, *Phys. Rev. Lett.* **2022**, *128*, 187801.
[30] J. Midya, Y. Cang, S. A. Egorov, K. Matyjaszewski, M. R. Bockstaller, A. Nikoubashman, G. Fytas, *Nano Lett.* **2019**, *19*, 2715.
[31] Y. Cang, A. N. Reuss, J. Lee, J. Yan, J. Zhang, E. Alonso-Redondo, R. Sainidou, P. Rembert, K. Matyjaszewski, M. R. Bockstaller, G. Fytas, *Macromolecules* **2017**, *50*, 8658.
[32] D. Schneider, M. Schmitt, C. M. Hui, R. Sainidou, P. Rembert, K. Matyjaszewski, M. R. Bockstaller, G. Fytas, *ACS Macro Lett.* **2014**, *3*, 1059.
[33] A. Halperin, M. Tirrell, T. P. Lodge, *Adv. Polym. Sci.* **1992**, *100*, 31.
[34] B. Zuo, C. Li, Q. Xu, K. Randazzo, N. Jiang, X. Wang, R. D. Priestley, *ACS Nano* **2021**, *15*, 9568.
[35] F. E. Bernardin, G. C. Rutledge, *Polymer* **2007**, *48*, 7211.
[36] C. A. Grabowski, H. Koerner, J. S. Meth, A. Dang, C. M. Hui, K. Matyjaszewski, M. R. Bockstaller, M. F. Durstock, R. A. Vaia, *ACS Appl. Mater. Interfaces* **2014**, *6*, 21500.
[37] C. Mahoney, C. M. Hui, S. Majumdar, Z. Wang, J. A. Malen, M. N. Tchoul, K. Matyjaszewski, M. R. Bockstaller, *Polymer* **2016**, *93*, 72.
[38] K. Ohno, T. Morinaga, S. Takeno, Y. Tsujii, T. Fukuda, *Macromolecules* **2006**, *39*, 1245.
[39] J. Lee, Z. Wang, J. Zhang, J. Yan, T. Deng, Y. Zhao, K. Matyjaszewski, M. R. Bockstaller, *Macromolecules* **2020**, *53*, 1502.
[40] J. G. Ethier, L. M. Hall, *Macromolecules* **2018**, *51*, 9878.
[41] C. Rossner, Q. Tang, O. Glatter, M. Müller, P. Vana, *Langmuir* **2017**, *33*, 2017.
[42] C. M. Hui, J. Pietrasik, M. Schmitt, C. Mahoney, J. Choi, M. R. Bockstaller, K. Matyjaszewski, *Chem. Mater.* **2014**, *26*, 745.
[43] J. Yan, M. R. Bockstaller, K. Matyjaszewski, *Prog. Polym. Sci.* **2020**, *100*, 101180.
[44] C. N. Likos, H. Löwen, M. Watzlawek, B. Abbas, O. Jucknischke, J. Allgaier, D. Richter, *Phys. Rev. Lett.* **1998**, *80*, 4450.
[45] I. E. Psarobas, N. Stefanou, A. Modinos, *Phys. Rev. B* **2000**, *62*, 278.
[46] R. Sainidou, N. Stefanou, I. E. Psarobas, A. Modinos, *Comput. Phys. Commun.* **2005**, *166*, 197.
[47] W. Huang, S. I. Rokhlin, Y. J. Wang, *J. Acoustical Soc. Am.* **1997**, *101*, 2031.